Thermally activated flux motion in optimally electron-doped $(Ca_{0.85}La_{0.15})_{10}(Pt_3As_8)(Fe_2As_2)_5$ and $Ca_{10}(Pt_3As_8)((Fe_{0.92}Pt_{0.08})_2As_2)_5$ single crystals

W.J. Choi, Y.I. Seo, D. Ahmad, Yong Seung Kwon[*]

Department of Emerging Materials Science, DGIST, Daegu 711-873, Republic of Korea

ABSTRACT

The temperature dependence of the electric resistivity measured in various magnetic fields was analyzed by the vortex glass theory and the thermally activated flux motion (TAFM) theory. The vortex glass-to-vortex liquid (GTL) transition T_g obtained from the analysis shows a temperature dependence of $B_g(T) = B_0(1 - T/T_c)^m$. The vortex liquid region is divided into the critical region existing in a finite temperature region just above T_g and the TAFM region present in the finite temperature region above it. In the critical region, the activation energy is expressed as $U_{eff} = k_B T(T_c - T)/(T_c - T_g)$, whereas in the TAFM region, the activity energy is expressed as temperature-nonlinear $U(T, B) = U_0(B)(1 - t)^q$. In the GTL transition, $(Ca_{0.85}La_{0.15})_{10}(Pt_3As_8)(Fe_2As_2)_5$ maintains the 3D vortex structure without exhibiting dimension crossover of the vortex, but $Ca_{10}(Pt_3As_8)((Fe_{0.92}Pt_{0.08})_2As_2)_5$ exhibits the dimension crossover from the 3D vortex glass to the 2D vortex liquid.

Introduction

The $Ca_{10}(Pt_3As_8)(Fe_2As_2)_5$ system attracts a lot of attention as a rare class of iron based superconductor that exhibits superconductivity with semiconductor electrical properties due to local electrons [1]. The optimally electron-doped $(Ca_{0.85}La_{0.15})_{10}(Pt_3As_8)(Fe_2As_2)_5$ and $Ca_{10}(Pt_3As_8)((Fe_{0.92}Pt_{0.08})_2As_2)_5$ single crystals raise critical temperatures to about 32 and 13 K, respectively. This system also exhibits other iron-based superconductor properties such as multiband nature [2,3], high upper critical field [4,5], and high critical current [6]. In addition, this system has a high anisotropy, $\gamma \sim 6.7$ for the former [4] and ~10.2 for the latter [5], near T_c and a very high penetration depth [2,7] and low superfluid density [7,8].

The $Ca_{10}(Pt_3As_8)(Fe_2As_2)_5$ system has a layered Ca-(Pt_3As_8)-Ca-(Fe_2As_2) stack [1]. The Ca layer acts as a charge reservoir, and the intermediary Pt_3As_8 layer serves to control the superconducting coupling between the superconducting layer Fe_2As_2. This structure is similar to cuprates having intermediary layers [9], especially $Bi_2Sr_2Ca_{n-1}Cu_nO_{2n+4+x}$. In $Bi_2Sr_2Ca_{n-1}Cu_nO_{2n+4+x}$, it has been proposed that the high T_c is controlled by the change of coupling between CuO_2 planes through the intercalation of the intermediate layer [10–13]. In this sense, the $Ca_{10}(Pt_3As_8)(Fe_2As_2)_5$ system is one of the key

candidates to provide an important clue to understanding high-T_c superconductivity. For a comprehensive understanding of superconductivity in this system, vortex dynamics by thermal fluctuation, along with determination of parameters such as high upper critical fields, is also very important. In the mixed state, thermal fluctuations directly affect the vortex motion by thermally activated flux motion (TAFM) and lead tails in the superconducting transition.

The magnitude of thermal fluctuation is quantified by the Ginzburg number, $G_i = 10^{-9}(\kappa^4 T_c \gamma^2 / H_{c2}(0))^2$, where $\kappa = \lambda_0 / \xi_0$ is the Ginzburg-Landau parameter (λ_0 is the London penetration depth and ξ_0 is the superconducting coherence length) , $\gamma = \xi_{ab} / \xi_c$ is the anisotropy ratio, T_c is the critical temperature in unit of K and $H_{c2}(0)$ is the zero-temperature upper critical field in unit of Oe. The Ginzburg number is $G_i \sim 10^{-8} - 10^{-5}$ for conventional low-T_c superconductors, while $G_i \sim 10^{-2} - 10^{-1}$ for high-T_c cuprates [14]. Strong thermal fluctuations induce various vortex phases and vortex dynamics in high-T_c cuprates. In iron-based superconductors, for $SmFeAs(O_{1-x}F_x)$, $G_i \sim 1 \times 10^{-2}$ showed almost the same magnitude as cuprates [15], and many studies have been conducted to study various vortex phases and dynamics [16–19]. The $(Ca_{0.85}La_{0.15})_{10}(Pt_3As_8)(Fe_2As_2)_5$ and $Ca_{10}(Pt_3As_8)((Fe_{0.92}Pt_{0.08})_2As_2)_5$ single crystals studied here show $G_i \sim 1.5 \times 10^{-2}$ [2,4] and $G_i \sim 3 \times 10^{-2}$ [5,20], respectively, which equivalent to or larger than that of SmFeAs

$(O_{1-x}F_x)$, one of the samples with the largest value of G_i in iron-based superconductors. Therefore, these samples are expected to show various vortex phases and vortex dynamics due to strong thermal fluctuations.

In this study, the electrical resistivity under a magnetic field was measured with high precision in $(Ca_{0.85}La_{0.15})_{10}(Pt_3As_8)(Fe_2As_2)_5$, substituted with La ions instead of Ca ions in the charge reservoir Ca layer, and $Ca_{10}(Pt_3As_8)((Fe_{0.92}Pt_{0.08})_2As_2)_5$, substituted with Pt ions instead of Fe ions in the superconducting (Fe_2As_2) layer, to study their vortex phase and vortex dynamics. In this analysis, the magnetic field dependence of zero-temperature activation energy is determined based on the TAFM theory. In addition, the vortex glass-to-vortex liquid (GTL) transition temperature T_g showing the zero electrical resistivity is observed at a lower temperature, and a critical region represented by the effective activation energy, which is different from the activation energy in the vortex liquid phase, exists just above T_g.

Experimental details

Single crystals of $(Ca_{0.85}La_{0.15})_{10}(Pt_3As_8)(Fe_2As_2)_5$ and $Ca_{10}(Pt_3As_8)((Fe_{0.92}Pt_{0.08})_2As_2)_5$ were grown by a Bridgman method and self-flux method, respectively. The precursors of CaAs, LaAs and FeAs were synthesized in evacuated quartz ampoules at 550, 800 and 1050 °C, respectively. The growth of $(Ca_{0.85}La_{0.15})_{10}(Pt_3As_8)(Fe_2As_2)_5$ single crystal is as follows: the powders of CaAs, LaAs, FeAs and Pt were mixed in the mortar, and then the mixture was placed in a BN crucible. Then, BN crucible was placed in a Mo crucible to prevent reaction of between the mixture and metal crucible. The whole procedure was carried out in a glove box under an Ar gas atmosphere. The Mo crucible was sealed with an arc welder under an Ar gas. The welded Mo crucible was placed in a high-vacuum electric furnace having a high temperature stability of ± 0.1 °C and a single crystal was grown at 1250 °C. The typical size of $(Ca_{0.85}La_{0.15})_{10}(Pt_3As_8)(Fe_2As_2)_5$ single crystals is $\sim 2 \times 2 \times 0.5$ mm^3. For the single crystals of $Ca_{10}(Pt_3As_8)((Fe_{0.92}Pt_{0.08})_2As_2)_5$, the precursors of CaAs and FeAs were used as self-flux for single crystal growth. These precursors and Pt powder were mixed well in the mortar according to the ratio of CaAs : FeAs : Pt = 2 : 2 : 1. The weighed mixture was placed in a BN crucible and put in a quartz ampoule. This whole procedure was carried out in a glove box. The quartz ampoule was sealed under high vacuum. The sealed ampoule was slowly heated to 1150 °C, maintained for 5 days, slowly cooled to 850 °C at a rate of 3 °C/ h, followed by water quenching immediately. Since CaAs flux is sensitive to air and moisture, single crystals can be easily obtained by naturally decomposing the bulk in the air for a day. The thickness of the single crystals obtained by self-flux method is thinner than $(Ca_{0.85}La_{0.15})_{10}(Pt_3As_8)(Fe_2As_2)_5$ single crystal grown by the Bridgman method, and the typical size of the sample is $\sim 2 \times 2 \times 0.1$ mm^3.

The in-plane electrical resistivity on $B//c$-axis in the single crystals were performed by using an Oxford superconducting system. The electrical resistivity was measured by a standard four-probe method at a current density of ~ 20 A/cm^2. The surface of the samples was patterned with four gold electrodes using Au evaporation to reduce the contact resistance, and gold wire was attached to the electrodes using silver epoxy (EPO-TEK H20E). The contact resistance was below 1 Ω. The temperature dependence of the electrical resistivity was measured from 2 to 85 K at about 0.04 K intervals under applied magnetic fields of $B =$ 0, 0.5, 1, 1.5, 2, 3, 4, 5 and 6 T.
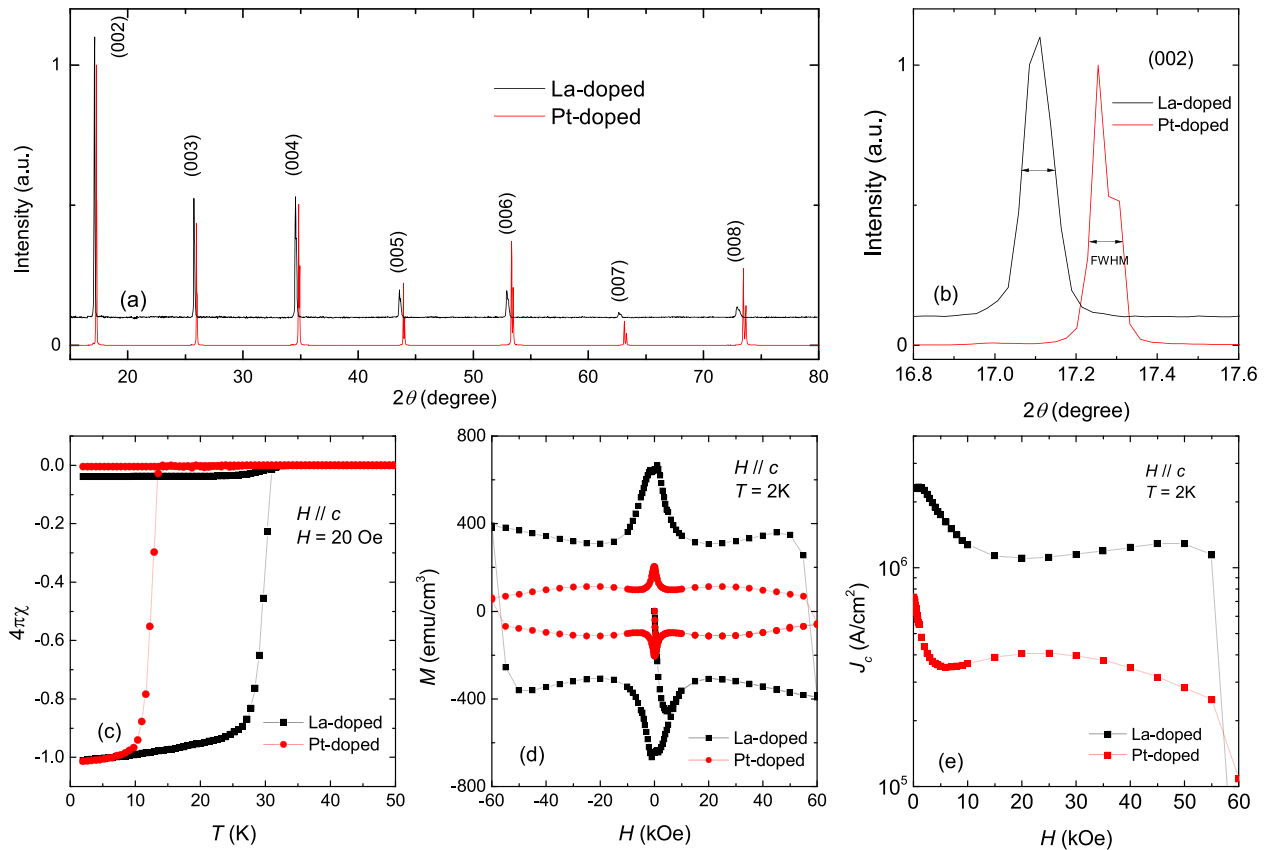

Fig. 1. (a) XRD pattern of the $(Ca_{0.85}La_{0.15})_{10}(Pt_3As_8)(Fe_2As_2)_5$ and $Ca_{10}(Pt_3As_8)((Fe_{0.92}Pt_{0.08})_2As_2)_5$ single crystals. (b) The inset is a magnified (0 0 2) peak. (c) Temperature dependence of ZFC and FC magnetic susceptibility measured at $H = 20$ Oe for $H//c$ in $(Ca_{0.85}La_{0.15})_{10}(Pt_3As_8)(Fe_2As_2)_5$ and $Ca_{10}(Pt_3As_8)((Fe_{0.92}Pt_{0.08})_2As_2)_5$ single crystals. (d) Magnetic field dependence of magnetization $M(H)$ and (e) critical current $J_c(H)$ of $(Ca_{0.85}La_{0.15})_{10}(Pt_3As_8)(Fe_2As_2)_5$ and $Ca_{10}(Pt_3As_8)((Fe_{0.92}Pt_{0.08})_2As_2)_5$ single crystals at 2 K for $H//c$.

Results and discussion

The XRD results for $(Ca_{0.85}La_{0.15})_{10}(Pt_3As_8)(Fe_2As_2)_5$ and $Ca_{10}(Pt_3As_8)((Fe_{0.92}Pt_{0.08})_2As_2)_5$ single crystals are shown in Fig. 1(a). In both samples, only (00ℓ) oriented peaks are observed, indicating that the c-axis of the single crystal is perpendicular to the plane where the x-ray is incident, and that there is no secondary phase. Each peak shows a double peak structure because the used x-ray is composed of Cu-$K_{\alpha1}$ and Cu-$K_{\alpha2}$. The interplanar distance d of the Fe_2As_2 layer evaluated from these peaks is 10.371 and 10.301 Å in $(Ca_{0.85}La_{0.15})_{10}(Pt_3As_8)(Fe_2As_2)_5$ and $Ca_{10}(Pt_3As_8)((Fe_{0.92}Pt_{0.08})_2As_2)_5$, respectively, which is almost similar to the reported results [4,6]. Also, as seen in Fig. 1(b), the full width at half maximum of the peaks is very narrow as FWHM $\sim 0.1°$, which indicates that the single crystal is well aligned.

The temperature dependence of zero-field-cooled (ZFC) and field-cooled (FC) magnetization measured at $H = 20$ Oe for $H//c$ in $(Ca_{0.85}La_{0.15})_{10}(Pt_3As_8)(Fe_2As_2)_5$ and $Ca_{10}(Pt_3As_8)((Fe_{0.92}Pt_{0.08})_2As_2)_5$ is shown in Fig. 1(c). $(Ca_{0.85}La_{0.15})_{10}(Pt_3As_8)(Fe_2As_2)_5$ and $Ca_{10}(Pt_3As_8)((Fe_{0.92}Pt_{0.08})_2As_2)_5$ exhibit diamagnetic onsets at 31.5 and 13.5 K and then reach full magnetization at about 25 and 9 K, respectively. The full magnetization in both samples corresponds to $4\pi\chi = -1$, indicating that both samples exhibit perfect diamagnetism due to bulk superconductivity. Fig. 1(d) shows the magnetization $M(H)$ as a function of the magnetic field at 2 K for $H//c$ in $(Ca_{0.85}La_{0.15})_{10}(Pt_3As_8)(Fe_2As_2)_5$ and $Ca_{10}(Pt_3As_8)((Fe_{0.92}Pt_{0.08})_2As_2)_5$. $M(H)$ in both samples show magnetization hysteresis loops. We evaluated the critical current $J_c(H)$ at 2 K using the Beans model [21] from their magnetization hysteresis loops. The evaluated $J_c(0)$ is 7.3×10^5 and 2.3×10^6 A/cm^2 for $Ca_{10}(Pt_3As_8)((Fe_{0.92}Pt_{0.08})_2As_2)_5$ and $(Ca_{0.85}La_{0.15})_{10}(Pt_3As_8)(Fe_2As_2)_5$, respectively. $J_c(0)$ of the former is about three times larger than that of Pt-overdoped $Ca_{10}(Pt_3As_8)((Fe_{0.895}Pt_{0.105})_2As_2)_5$ [6], and $J_c(0)$ of latter is about 1/2 compared to that in K-doped Ba122 with similar T_c [22]. The $M(H)$ curves for both samples show a second peak called a fishtail. The fishtail effect has been observed in other iron-based superconductors, where it has been interpreted as a crossover from vortex elastic to plastic deformation [23]. Analysis at detailed temperatures is required to check the validity of the crossover model in our sample.

Fig. 2(a) and (b) show the temperature dependence of the in-plane electrical resistivity of $(Ca_{0.85}La_{0.15})_{10}(Pt_3As_8)(Fe_2As_2)_5$ and $Ca_{10}(Pt_3As_8)((Fe_{0.92}Pt_{0.08})_2As_2)_5$ single crystals on a semi-logarithmic scale measured under a magnetic field applied along the c-axis, respectively. The superconducting critical temperature in the zero magnetic field is about $T_c^{off} = 32.2$ K and 13.2 K, respectively, which is consistent with the results of the magnetic susceptibility described above. Since the electrical resistivity bends downward as the temperature decreases in the normal state, the superconducting transition width ΔT_c was determined from twice the temperature difference corresponding to 0–50% of the normal state electrical resistivity value: $\Delta T_c = 0.5$ K for the former and $\Delta T_c = 0.6$ K for the latter.

As shown in Fig. 2(a) and (b), the electrical resistivity due to the transition to the superconducting state shows typical broadening as the magnetic field increases due to thermally activated flux motion (TAFM). The activation energy U_0 for the flux motion is usually determined by linear fitting in the appropriate temperature range in each Arrhenius plot. This analysis is only valid for the linear temperature dependent activation energy, $U(T,B) = U_0(B)(1-t)$, where $t = T/T_c$. In this case, $U_a = -\partial \ln\rho/\partial(1/T)$ is constant with temperature changes. As shown in Fig. 3(a) and (b), U_a for the samples studied here is completely different from that. To further solve this problem, we also conduct a study on TAFM of the studied sample through a method performed earlier by Zhang et al. [24,25]. For the thermally activated flux motion, the electrical resistivity is given by

$$\rho(T) = (2\rho_c U(B,T)/T)\exp(-U(B,T)/T) \tag{1}$$

Prefacter $\rho_{0f} = 2\rho_c U(B,T)/T$ is generally temperature dependent, but in the analysis of many high-T_c superconductors it was assumed to be constant. The activation energy is given as a nonlinear $U(T,B) = U_0(B)(1-t)^q$. Using this, Eq. (1) is given by

$$D = \ln\rho(T) = \ln(2\rho_c U_0(B)) + q\ln(1-t) - \ln T - U_0(B)(1-t)^q/T \tag{2}$$

and the derivative of Eq. (2) as $1/T$ is given by

$$U_a = -\partial \ln\rho/\partial(1/T) = [U_0(B)(1-t)^q - T][1 + qt/(1-t)] \tag{3}$$

The solid green line in Fig. 3(a) and (b) is the best fits for U_a at 6 T with Eq. (3) in $(Ca_{0.85}La_{0.15})_{10}(Pt_3As_8)(Fe_2As_2)_5$ and $Ca_{10}(Pt_3As_8)((Fe_{0.92}Pt_{0.08})_2As_2)_5$, respectively, and the solid green line in Fig. 4(a) and (b) shows the best fits corresponding to the data measured in each magnetic field. The best fit agrees well with the experimental values only in a limited temperature range. The best fits were achieved with T_c
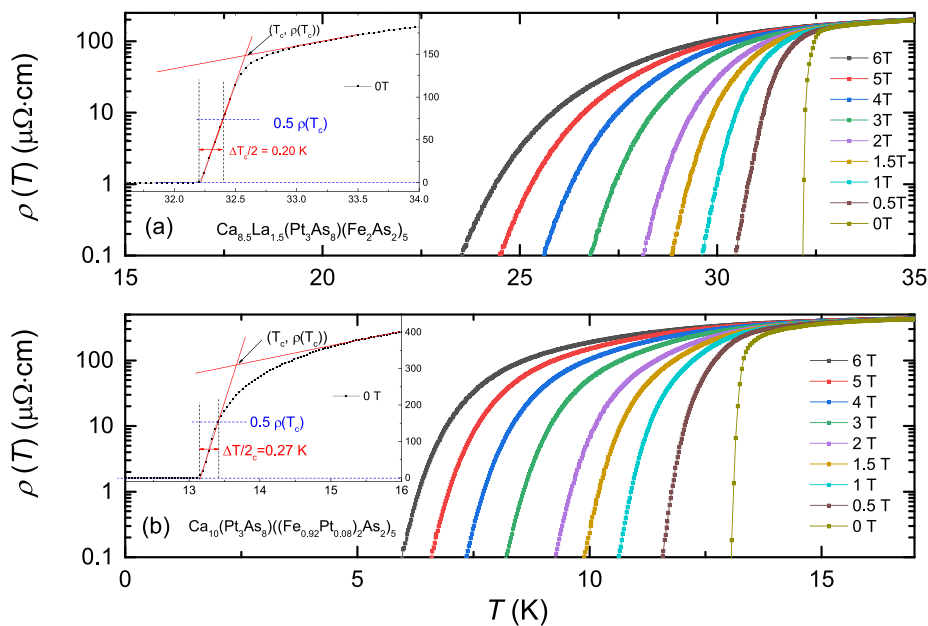

Fig. 2. (a) and (b): temperature dependent electrical resistivity with various applied magnetic fields along c-axis for $(Ca_{0.85}La_{0.15})_{10}(Pt_3As_8)(Fe_2As_2)_5$ and $Ca_{10}(Pt_3As_8)((Fe_{0.92}Pt_{0.08})_2As_2)_5$ single crystals, respectively. Inset: temperature dependent electrical resistivity near T_c for the samples.
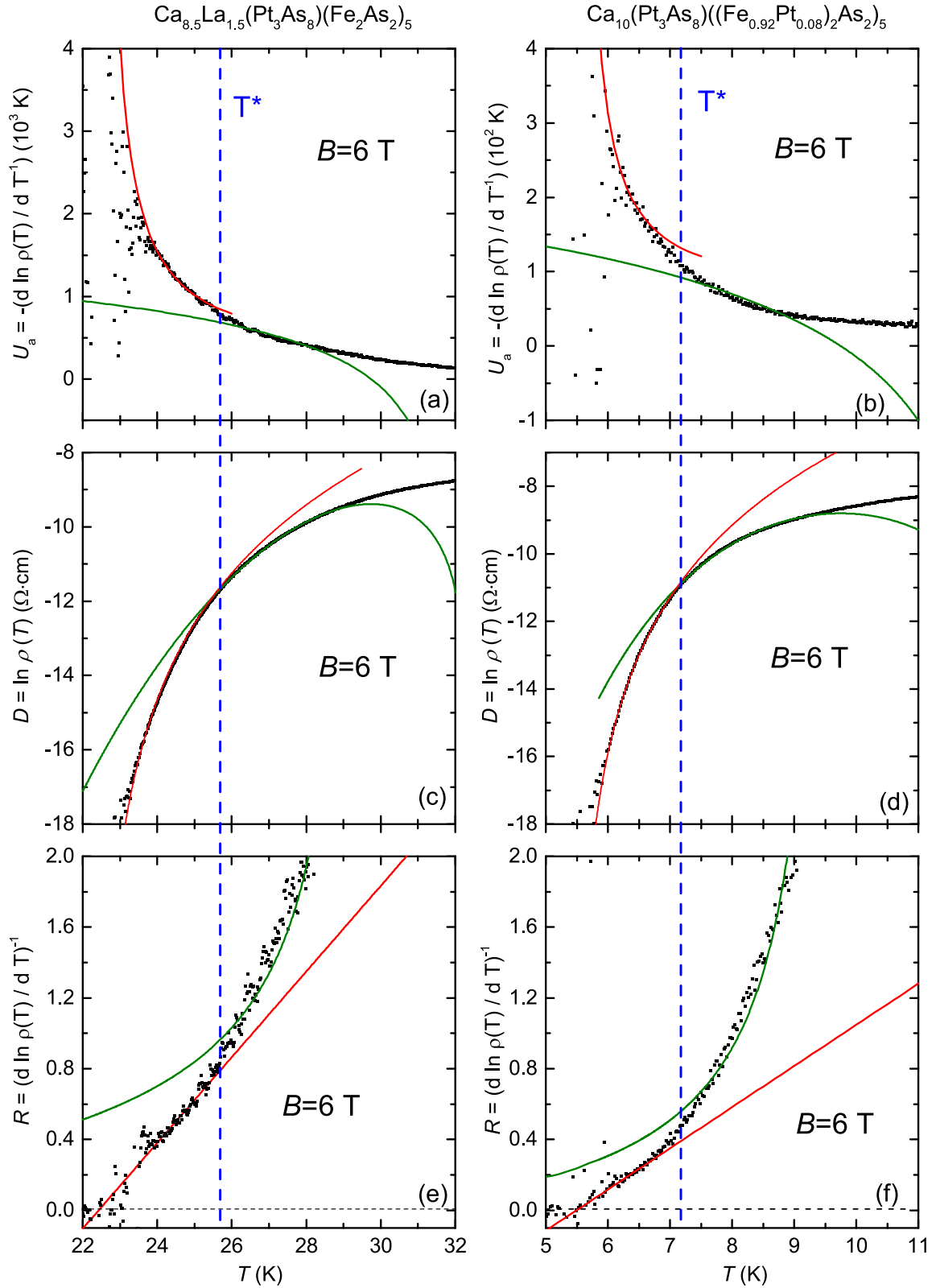
Fig. 3. Derivatives from in-plane electrical resistivity measured on $(Ca_{0.85}La_{0.15})_{10}(Pt_3As_8)(Fe_2As_2)_5$ and $Ca_{10}(Pt_3As_8)((Fe_{0.92}Pt_{0.08})_2As_2)_5$ single crystals at $B = 6$ T. (a) and (b): derivatives $U_a = (d\ln\rho(T))/(dT^{-1})$ for the former and the latter, respectively. The green line is the fit according to Eq. (3), and the red line is the fit according to the expression $\rho(T) = \rho_n[\exp(U_{eff}/k_BT)]^s$ with $U_{eff} = k_BT(T_c - T)/(T_c - T_g)$. (c) and (d): derivatives $D = \ln\rho(T)$ for the former and the latter, respectively. The green line is the fit according to Eq. (2), and the red line is the fit according to the expression $\rho(T) = \rho_n[\exp(U_{eff}/k_BT)]^s$ with $U_{eff} = k_BT(T_c - T)/(T_c - T_g)$. (e) and (f): derivatives $R = (d\ln\rho(T)/dT)^{-1}$ for the former and the latter, respectively. The red line is the fit according to TAFM model, and the green line is fit according to Eq. (4). (For interpretation of the references to colour in this figure legend, the reader is referred to the web version of this article.)
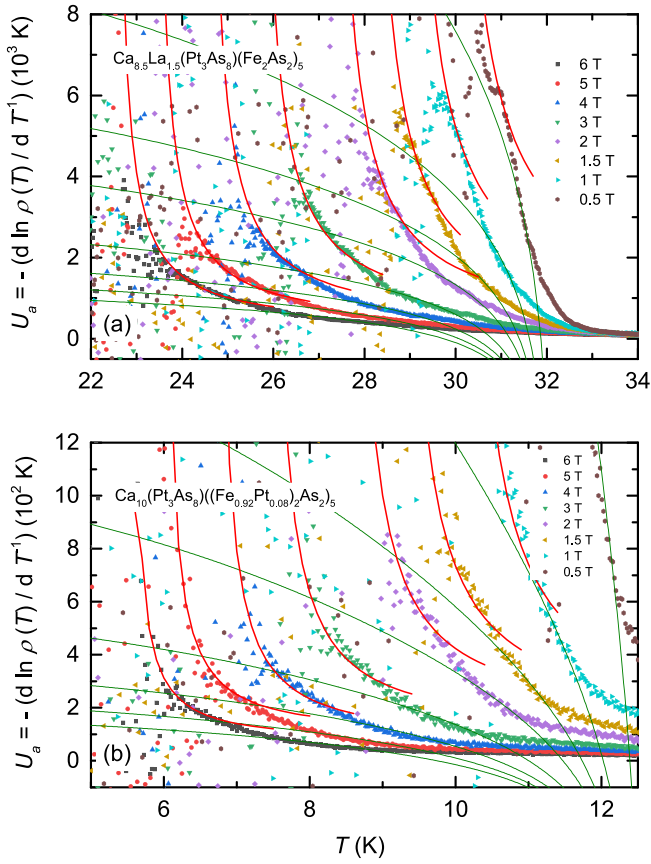
Fig. 4. (a) and (b): temperature dependence of $U_a = (d\ln\rho(T))/(dT^{-1})$ for various magnetic fields in $(Ca_{0.85}La_{0.15})_{10}(Pt_3As_8)(Fe_2As_2)_5$ and $Ca_{10}(Pt_3As_8)((Fe_{0.92}Pt_{0.08})_2As_2)_5$ single crystals, respectively. The green line is the fit according to Eq. (3), and the red line is the fit according to the expression $\rho(T) = \rho_n[\exp(U_{eff}/k_BT)]^s$ with $U_{eff} = k_BT(T_c-T)/(T_c-T_g)$. (For interpretation of the references to colour in this figure legend, the reader is referred to the web version of this article.)

Fig. 5. (a) and (b): $D = \ln\rho(T)$ vs. $1/T$ plots for various magnetic fields in $(Ca_{0.85}La_{0.15})_{10}(Pt_3As_8)(Fe_2As_2)_5$ and $Ca_{10}(Pt_3As_8)((Fe_{0.92}Pt_{0.08})_2As_2)_5$ single crystals, respectively. The green line is the fit according to Eq. (2), and the red line is the fit according to the expression $\rho(T) = \rho_n[\exp(U_{eff}/k_BT)]^s$ with $U_{eff} = k_BT(T_c-T)/(T_c-T_g)$. (For interpretation of the references to colour in this figure legend, the reader is referred to the web version of this article.)

$= 32.3$ K and $q = 1.52$ for $(Ca_{0.85}La_{0.15})_{10}(Pt_3As_8)(Fe_2As_2)_5$ and $T_c = 12.8$ K and $q = 2$ for $Ca_{10}(Pt_3As_8)((Fe_{0.92}Pt_{0.08})_2As_2)_5$. In Fig. 3(c) and (d), the green solid line shows the best fit for D at 6 T with Eq. (2) in $(Ca_{0.85}La_{0.15})_{10}(Pt_3As_8)(Fe_2As_2)_5$ and $Ca_{10}(Pt_3As_8)((Fe_{0.92}Pt_{0.08})_2As_2)_5$, respectively, and the green solid line in Fig. 5(c) and (d) shows the best fits corresponding to the data measured in each magnetic field. These best fits agree well with the experimental values in the fitting temperature range using Eq. (3). The best fits in both methods above were achieved with the same values for fitting parameters. The zero-temperature activation energy $U_0(B)$ determined by both methods was also the same, which is shown in Fig. 6(a) and (b) for $(Ca_{0.85}La_{0.15})_{10}(Pt_3As_8)(Fe_2As_2)_5$ and $Ca_{10}(Pt_3As_8)((Fe_{0.92}Pt_{0.08})_2As_2)_5$, respectively, as log–log scales. In both samples, the zero-temperature activation energy shows the dependency of $U_0(B)\sim B^{-\alpha}$ with $\alpha = 1.11$ for the former and $\alpha = 1.68$ for the latter in the entire measured magnetic field region. The behavior of $U_0(B)\sim B^{-\alpha}$ can be understood by plastic creep theory [26]. According to the plastic flux creep model, $U_0(B)\sim B^{-0.5}$ are predicted by the plastic deformation or entanglement of vortex lines in vortex liquid weakly pinned to point defects. Cutting or reconnecting the vortex lines that occur due to the relative movement between such entangled vortex lines changes the motion of the vortices, so the exponent can change within a certain range. As an example, $\alpha \sim 0.7$ in untwinned YBCO was observed by the vortex entanglement in weakly pinned vortex liquid [27]. A larger exponent is expected by entanglement of vortex lines in vortex liquid strongly pinned to point defects [27].
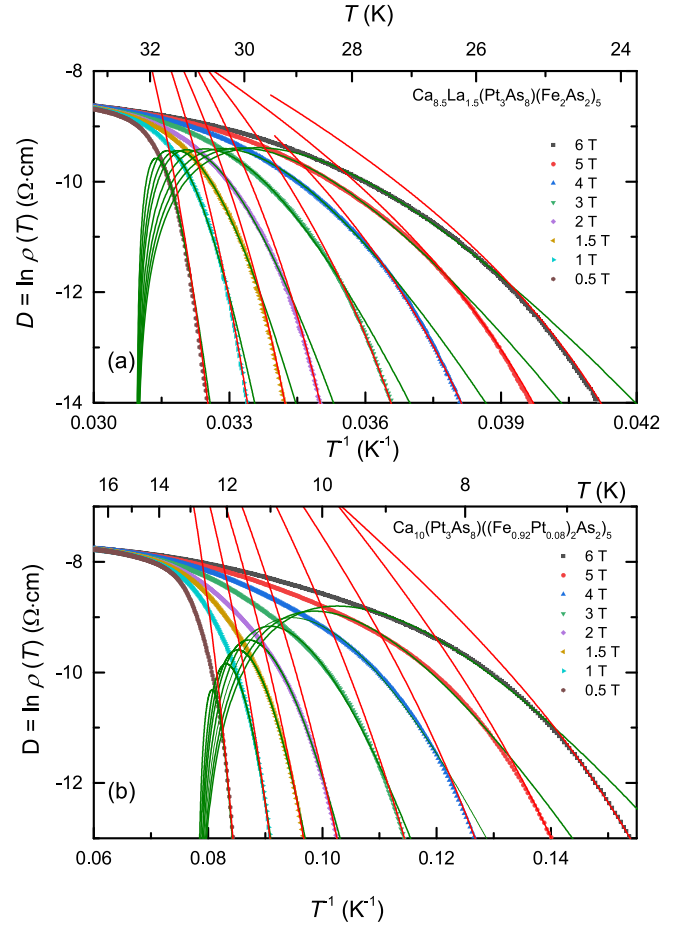
Based on this theory, it can be thought that point defects mainly caused by heteroatoms doped in our samples play an important role in vortex pinning and lead to weakly or strongly entangled vortices depending on the strength of the magnetic field. The exponent in these two samples is significantly larger than 0.7 for the weak pinning described just above, so the magnetic field dependence of the activation energy in both samples can be expected to be caused by strong pinning in the measured magnetic field region. This strong pinning will be discussed just below, but it is also inferred from the large U_0 in a low magnetic field compared to similar T_c materials. As the magnetic field increases in the measured magnetic field region, the plastic deformation or entanglement of the vortex lines leads to a reduced correlation length along the vortex line, resulting in a decrease in activation energy due to weakened vortex line coupling. A larger exponent α in the $Ca_{10}(Pt_3As_8)((Fe_{0.92}Pt_{0.08})_2As_2)_5$ sample compared to $(Ca_{0.85}La_{0.15})_{10}(Pt_3As_8)(Fe_2As_2)_5$ means that the vortex lines are more entangled according to this theory. This strong entanglement causes a shorter correlation length along the vortex line in $Ca_{10}(Pt_3As_8)((Fe_{0.92}Pt_{0.08})_2As_2)_5$. This produces larger anisotropy in the $Ca_{10}(Pt_3As_8)((Fe_{0.92}Pt_{0.08})_2As_2)_5$, which is well consistent with the reported results [4,5]. The stronger anisotropy in $Ca_{10}(Pt_3As_8)((Fe_{0.92}Pt_{0.08})_2As_2)_5$ causes $q = 2$, unlike the $q = 1.52$ observed in $(Ca_{0.85}La_{0.15})_{10}(Pt_3As_8)(Fe_2As_2)_5$. In general, $q = 1.5$ is observed in high-T_c superconductors such as LiFeAs [28] and YBCO [29] showing 3D behaviors, while $q = 2$ is observed in high-T_c superconductors such as $SmFeAs_{0.9}F_{0.1}$ [25], GdBCO [30] and $Tl_2Ba_2CaCu_2O_x$
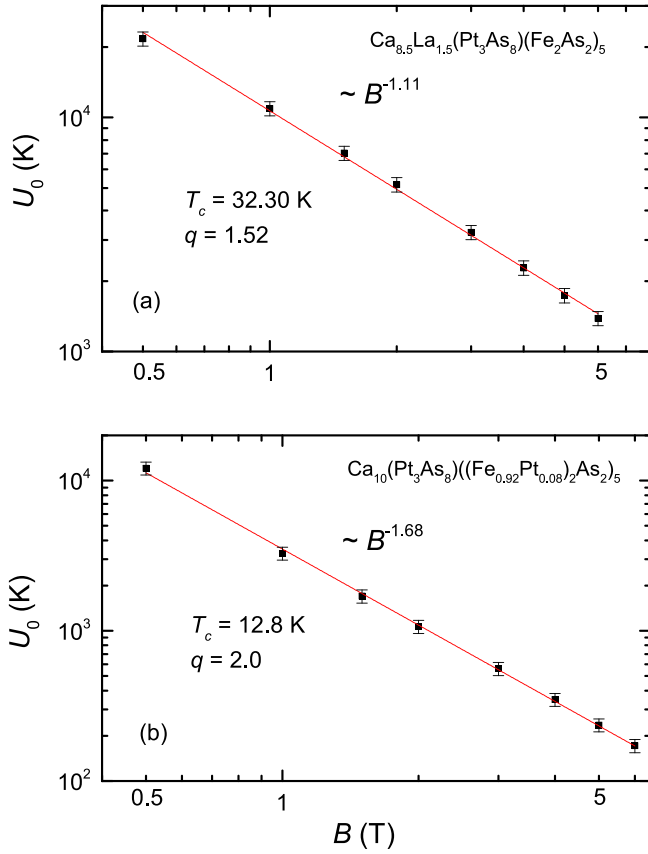
Fig. 6. (a) and (b): magnetic field dependence of thermal activation energy U_0 on flux motion when $B//c$ in $(Ca_{0.85}La_{0.15})_{10}(Pt_3As_8)(Fe_2As_2)_5$ and $Ca_{10}(Pt_3As_8)$ $((Fe_{0.92}Pt_{0.08})_2As_2)_5$ single crystals, respectively. The red line is a linear fit. (For interpretation of the references to colour in this figure legend, the reader is referred to the web version of this article.)

[31], which show strong 2D behaviors. Let's compare these U_0 and α values at $B = 1$ T with those of other iron-based high-T_c superconductors with similar T_c to our samples. As shown in Fig. 6, $(Ca_{0.85}La_{0.15})_{10}(Pt_3As_8)(Fe_2As_2)_5$ represents $U_0 \sim 11000$ K at $B = 1$ T and $Ca_{10}(Pt_3As_8)((Fe_{0.92}Pt_{0.08})_2As_2)_5$ represents $U_0 \sim 3000$ K. First, in superconductors with T_c similar to that of the former, $CeFeAsO_{0.85}F_{0.15}$ ($T_c \sim 33$ K) shows $U_0 \sim 1400$ K with $\alpha \sim 0.5$ [32], $Ba_{0.72}K_{0.28}Fe_2As_2$ ($T_c \sim 32$ K) shows $U_0 \sim 5000$ K with $\alpha \sim 0.2$ [33], and $Ca_{0.82}La_{0.18}FeAs_2$ ($T_c \sim 39$ K) shows $U_0 \sim 8500$ K with $\alpha \sim 0.34$ [34]. Compared to these materials, U_0 and α found in $(Ca_{0.85}La_{0.15})_{10}(Pt_3As_8)(Fe_2As_2)_5$ is significantly larger, which indicates that the vortex lines in this sample is strongly pinned. Next, in a superconductor with T_c similar to that of the latter, $FeSe_{0.4}Te_{0.6}$ ($T_c \sim 14$ K) shows $U_0 \sim 1200$ K and $\alpha \sim 0.86$ [35], $Fe_{1+y}(Te_{1+x}S_x)_2$ ($T_c \sim 9$ K) shows $U_0 \sim 200$ K and $\alpha \sim 0.21$ [36], and $NaFe_{0.97}Co_{0.03}As$ ($T_c \sim 14$ K) shows $U_0 \sim 700$ K and $\alpha \sim 0.27$ [37]. Compared to these materials, the values of U_0 and α found in $(Ca_{0.85}La_{0.15})_{10}(Pt_3As_8)(Fe_2As_2)_5$ are more than twice as large. In addition to this, the underdoped $Ca_{10}(Pt_3As_8)((Fe_{1-x}Pt_x)_2As_2)_5$ with lower T_c = 9.5 K showed $U_0 \sim 2000$ K at 1 T and $U_0(B) \sim B^{-\alpha}$ with $\alpha \sim 1$ above 0.5 T, determined by magnetic susceptibility measurement [17]. The $U_0(B)$ behavior in the underdoped sample is similar to that of our optimally doped sample, but U_0 is significantly smaller and α is also significantly smaller. This difference may be caused by the difference in T_c and a doping amount of Pt. These results clearly indicate that our $Ca_{10}(Pt_3As_8)$ $((Fe_{0.92}Pt_{0.08})_2As_2)_5$ sample strongly pins the vortex compared to these reported samples. The difference in U_0 between $(Ca_{0.85}La_{0.15})_{10}(Pt_3As_8)$ $(Fe_2As_2)_5$ and $Ca_{10}(Pt_3As_8)((Fe_{0.92}Pt_{0.08})_2As_2)_5$ is closely related to T_c, but individual differences in defect density, defect location and pinning strength will certainly play a major role.

As shown in Fig. 3(a) and (b), $U_a(T)$, determined by experiments with $(Ca_{0.85}La_{0.15})_{10}(Pt_3As_8)(Fe_2As_2)_5$ and $Ca_{10}(Pt_3As_8)((Fe_{0.92}Pt_{0.08})_2As_2)_5$ respectively, begins to deviate upward from the green line of $U_a(T)$ interpreted as TAFM in the temperature region below T^* and then fluctuates significantly at lower temperatures. The fluctuation of $U_a(T)$ is caused by a measurement error due to close proximity to zero electrical resistance, indicating the presence of a second order phase transition from the vortex liquid phase to the vortex glass phase. From this point of view, the deviation of $U_a(T)$ below T^* is due to the increased effective activation energy caused by gradual vortex glass development as the temperature decreases in the vortex liquid phase, and this temperature region is called a critical region present in the vortex liquid phase. According to the vortex glass theory [38], the electrical resistivity in this critical region is completely zero at the T_g temperature while satisfying $\rho(T)$ $|T - T_g|^{\nu(z+2-d)}$, where d is the dimensionality of the sample ($d = 3$ in these two samples), ν is the static index for vortex-glass correlation length, and z is the dynamic index for correlation time. Therefore, the logarithmic differential of this electrical resistivity is linearly dependent on T, i.e.

$$R = \left(\frac{d\ln\rho(T)}{dT}\right)^{-1} = \frac{1}{s}(T - T_g) \tag{4}$$

where $s = \nu(z + 2\text{-}d)$ is the inverse of the slope of Eq. (4). The red solid line in Fig. 3(e) and (f) is the best fit for R at 6 T with Eq. (4) in $(Ca_{0.85}La_{0.15})_{10}(Pt_3As_8)(Fe_2As_2)_5$ and $Ca_{10}(Pt_3As_8)((Fe_{0.92}Pt_{0.08})_2As_2)_5$, respectively. The solid red line in Fig. 7(a) and (b) represents the corresponding best fits for R obtained from the data measured in each magnetic field. This fit agrees well within the higher temperature limit of T^*. R using the fitting values obtained from the TAFM model discussed above is drawn in green line in Fig. 3(e) and (f), and the results agree well with the experimental values above T^*. From the fitting using Eq. (4), the vortex glass temperature T_g and critical exponent s were evaluated, and the magnetic field dependence of T_g, which is denoted $B_g(T)$, and s is shown in Figs. 8(a)-(b) and 9(a)-(b), respectively.

According to Lie et al., the thermal activity energy in the critical region present in the vortex liquid phase is given as $U_{eff} = k_B T(T_c - T)/(T_c - T_g)$ and the electrical resistivity is given as $\rho(T) = \rho_n[\exp(U_{eff}/k_B T)]^s$, which is consistent with the vortex-glass theory [38,39]. This means that the electrical resistivity $\rho(T)$ can be scaled within this critical region for the temperature scale $(T - T_g)/(T_c - T_g)$. Fig. 10(a) and (b) show the scaling of electrical resistivity for $(Ca_{0.85}La_{0.15})_{10}(Pt_3As_8)(Fe_2As_2)_5$ and $Ca_{10}(Pt_3As_8)$ $((Fe_{0.92}Pt_{0.08})_2As_2)_5$, respectively. In this scaling, the T_g and T_c obtained by the fitting discussed above were used. Data for different magnetic fields are not scaled into one value, which means that the value of the exponent s depends on the magnetic field. The magnetic field dependence of the s value determined by this scaling is shown in blue solid squares in Fig. 9(a) and (b) for $(Ca_{0.85}La_{0.15})_{10}(Pt_3As_8)(Fe_2As_2)_5$ and $Ca_{10}(Pt_3As_8)((Fe_{0.92}Pt_{0.08})_2As_2)_5$, respectively. In both samples studied, these s values are in good agreement with the results determined from Eq. (4). The magnetic field dependence of exponent s has been found in many iron-based superconductors [40,41]. Using $\rho(T) = \rho_n[\exp(U_{eff}/k_B T)]^s$, T_c, T_g, and s obtained by the scaling, $U_a(T)$ and $D(T)$ calculated at 6 T are drawn with red solid lines in Fig. 3(a)-(b) and (c)-(d), respectively. These are well matched with experimental data in the critical region. $U_a(T)$ and $D(T)$ for each measured magnetic field are shown with red solid lines in Figs. 4(a)-(b) and 5(a)-(b), respectively.

Generally, in 3D vortex glass, the s value lies between 2.7 and 8.5 [26]. The s values for $(Ca_{0.85}La_{0.15})_{10}(Pt_3As_8)(Fe_2As_2)_5$ and $Ca_{10}(Pt_3As_8)$ $((Fe_{0.92}Pt_{0.08})_2As_2)_5$ increase slightly within the values seen in 3D vortex glass as the magnetic field decreases in both samples as shown in Fig. 9 (a) and (b), respectively. Therefore, $(Ca_{0.85}La_{0.15})_{10}(Pt_3As_8)(Fe_2As_2)_5$ undergoes a phase transition from 3D vortex glass with $s > 2.7$ to 3D vortex liquid $q = 1.52$ at T_g, which means that the 3D correlation created
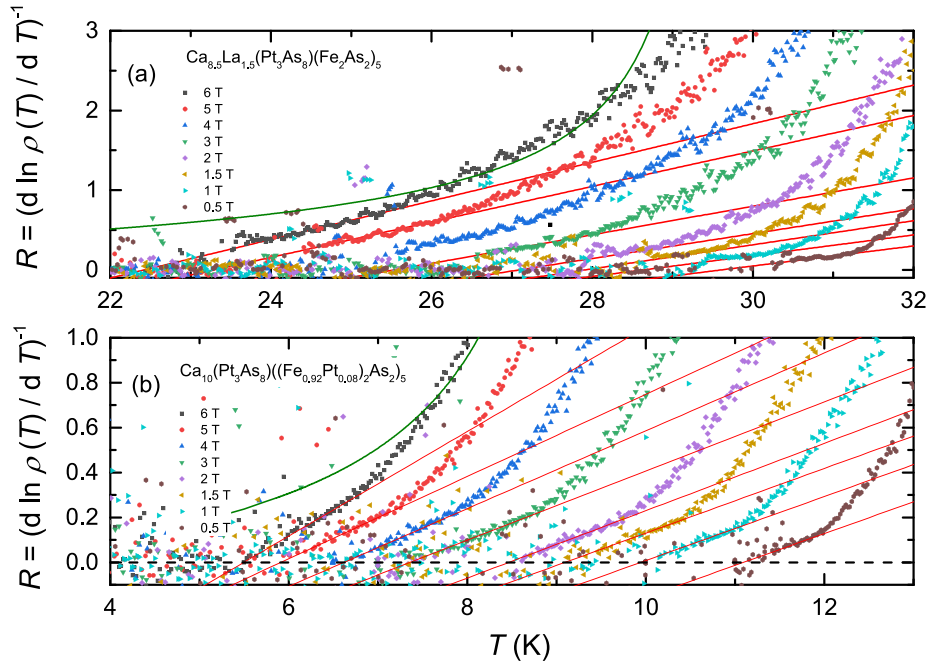
Fig. 7. (a) and (b): Temperature dependence of $R = (\mathrm{d\ln}\rho(T)/\mathrm{d}T)^{-1}$ at each magnetic field in $(Ca_{0.85}La_{0.15})_{10}(Pt_3As_8)(Fe_2As_2)_5$ and $Ca_{10}(Pt_3As_8)((Fe_{0.92}Pt_{0.08})_2As_2)_5$ single crystals, respectively. The red line is the fit according to TAFM model, and the green line is the fit according to Eq. (4). (For interpretation of the references to colour in this figure legend, the reader is referred to the web version of this article.)
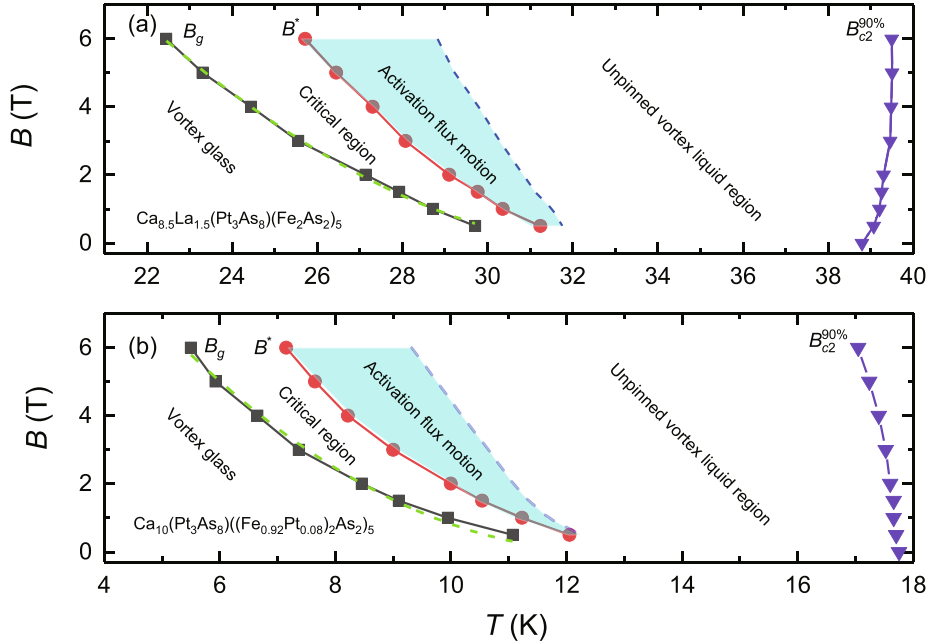

Fig. 8. (a) and (b): B-T phase diagram for $B//c$ in $(Ca_{0.85}La_{0.15})_{10}(Pt_3As_8)(Fe_2As_2)_5$ and $Ca_{10}(Pt_3As_8)((Fe_{0.92}Pt_{0.08})_2As_2)_5$ single crystals, respectively. The green dashed line is the fit according to $B_g(T) = B_0(1 - T/T_c)^m$. The blue dashed line indicates the separation of the thermal activation vortex liquid region and the flux flow region. (For interpretation of the references to colour in this figure legend, the reader is referred to the web version of this article.)

below T_g is maintained up to high temperature. Meanwhile, $Ca_{10}(Pt_3As_8)((Fe_{0.92}Pt_{0.08})_2As_2)_5$ undergoes a phase transition from 2D vortex liquid having $q = 2$ to 3D vortex glass having $s > 2.7$ at T_g. Physically speaking, for $Ca_{10}(Pt_3As_8)((Fe_{0.92}Pt_{0.08})_2As_2)_5$, when the pancake-like 2D vortex in the activation flux region above T^* enters the critical region just below T^*, it begins to transform into a disordered cylindric 3D vortex, which is further evolved below T_g, eventually creating 3D vortex glass. As discussed above, the dimensional difference between the two samples in the vortex liquid phase could be understood as the difference

in the magnitude of the anisotropy γ near T_c. The dimensional crossover found in $Ca_{10}(Pt_3As_8)((Fe_{0.92}Pt_{0.08})_2As_2)_5$ can also be understood as the temperature dependence of the γ-value. In this sense, $(Ca_{0.85}La_{0.15})_{10}(Pt_3As_8)(Fe_2As_2)_5$ seems to show very weak temperature dependence of anisotropy γ in the temperature range from T_c down to T_g, whereas $Ca_{10}(Pt_3As_8)((Fe_{0.92}Pt_{0.08})_2As_2)_5$ seems to significantly weaken the anisotropy as the temperature decreases in the temperature range. In order to confirm the dimensional crossover interpreted as the temperature dependence of the anisotropy, the band calculation using the first
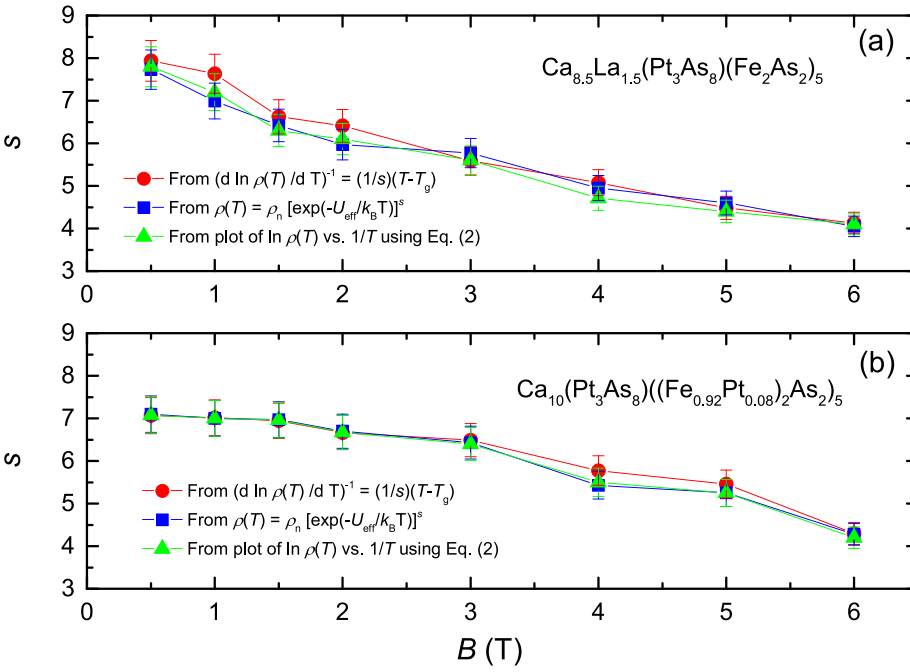
Fig. 9. (a) and (b): the magnetic field dependence of s when $B//c$ in $(Ca_{0.85}La_{0.15})_{10}(Pt_3As_8)(Fe_2As_2)_5$ and $Ca_{10}(Pt_3As_8)((Fe_{0.92}Pt_{0.08})_2As_2)_5$ single crystals, respectively. The red solid circle is the fit according to Eq. (4), the blue solid square is the fit according to the expression $\rho_n\left[\exp\left(U_{eff}/k_BT\right)\right]^s$ with $U_{eff} = k_BT(T_c - T)/(T_c - T_g)$, and green solid triangle is the fit according to Eq. (2). (For interpretation of the references to colour in this figure legend, the reader is referred to the web version of this article.)
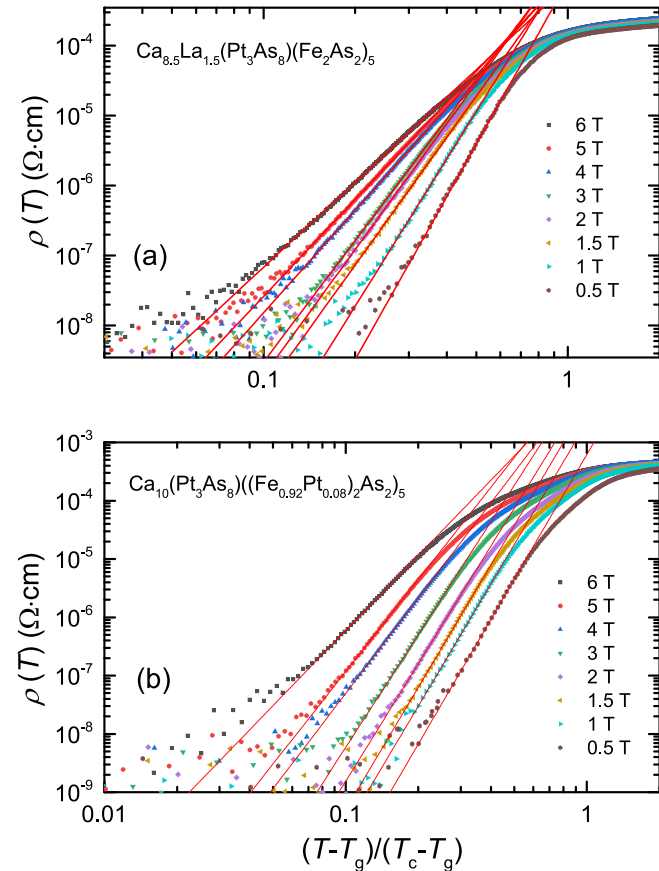

Fig. 10. (a) and (b): Scaling of temperature dependent electrical resistivity when $B//c$ in $(Ca_{0.85}La_{0.15})_{10}(Pt_3As_8)(Fe_2As_2)_5$ and $Ca_{10}(Pt_3As_8)((Fe_{0.92}Pt_{0.08})_2As_2)_5$ single crystals, respectively. Data in critical regions show power law behavior with exponent s. Here, the s value varies from 4 to 8 depending on the magnetic field.

principle method including the accurate many-body effect is required. $(Ca_{0.85}La_{0.15})_{10}(Pt_3As_8)(Fe_2As_2)_5$ with 3D vortex liquid is considered to be more advantageous in application than $Ca_{10}(Pt_3As_8)((Fe_{0.92}Pt_{0.08})_2As_2)_5$ with vortex-dimensional crossover, because 2D vortex liquid with large anisotropy causes easy energy dissipation due to more significant thermal fluctuation. A similar dimensional crossover in vortex was also observed in $Bi_2Sr_2CaCu_2O_{8+\delta}$ [42].

The B-T phase diagrams for the $B//c$-axis in $(Ca_{0.85}La_{0.15})_{10}(Pt_3As_8)(Fe_2As_2)_5$ and $Ca_{10}(Pt_3As_8)((Fe_{0.92}Pt_{0.08})_2As_2)_5$ are shown in Fig. 8 (a) and (b), respectively. Both samples show three distinct regions. GTL transition separates the vortex glass and vortex liquid regions into $B_g(T)$. This vortex glass line is well described as $B_g(T) = B_0(1 - T/T_c)^m$ with $B_0 = 47.5$ T and $m = 1.7$ for $(Ca_{0.85}La_{0.15})_{10}(Pt_3As_8)(Fe_2As_2)_5$ and $B_0 = 18.2$ T and $m = 2$ for $Ca_{10}(Pt_3As_8)((Fe_{0.92}Pt_{0.08})_2As_2)_5$, where B_0 is the zero-temperature vortex glass field and m is the exponent. The evaluated m values are similar to those for cuprates and iron-based superconductors [39,40,43]. The vortex liquid is divided into the critical region near T_g and the thermal activation region. These two regions are separated by $B*(T)$. Nevertheless, the critical region is well described by thermal activation with the effective pinning activation energy U_{eff} discussed above. The blue dashed line separating this thermal activation vortex liquid region and the unpinned vortex liquid region is obtained by the temperature at which the fitting green lines obtained with Eqs. (1) and (2) began to deviate from the measured data, as shown in Fig. 3 (a)-(d). The flux flow region is up to $B_{c2}^{90\%}$, which was determined with $90\% \cdot \rho_n$ criterion in Fig. 2 (a) and (b). For $(Ca_{0.85}La_{0.15})_{10}(Pt_3As_8)(Fe_2As_2)_5$, $B_{c2}^{90\%}$ increases as the temperature increases. As shown in Fig. 2, the significant round effect in the electrical resistivity near T_c caused a large error in determined $B_{c2}^{90\%}$, which is believed to have caused the increase in $B_{c2}^{90\%}$.

Conclusion

In summary, the temperature dependence of the detailed electrical resistivity under a magnetic field in $(Ca_{0.85}La_{0.15})_{10}(Pt_3As_8)(Fe_2As_2)_5$ and $Ca_{10}(Pt_3As_8)((Fe_{0.92}Pt_{0.08})_2As_2)_5$ single crystals with optimally doped electrons was measured to study the vortex phases and vortex dynamics. The vortex phases for the two samples are similarly divided into three vortex regions, but the temperature ranges in each region are

different for the two samples. The vortex glass region is well understood by the vortex glass theory with the 3D vortex glass. Vortex liquid regions are well described by thermally activated flux motion, but are divided into critical and activated flux motion regions due to the difference in temperature dependence of activation energy. The effective activation energy in critical region is given as $U_{eff} = k_B T(T_c - T)/(T_c - T_g)$, and the activation energy in the activated flux motion region is given by nonlinear $U(T,B) = U_0(B)(1 - t)^q$. The magnetic field dependence of zero-temperature activation energy shows the form of $U_0(B) \sim B^{-\alpha}$ from the low magnetic field. Compared to other iron-based superconductors, the evaluated U_0 is large in a low magnetic field and α is also large due to strongly pinned and entangled vortex lines. When the transition occurs from the vortex glass phase to the vortex liquid phase at T_g, $(Ca_{0.85}La_{0.15})_{10}(Pt_3As_8)(Fe_2As_2)_5$ maintains 3D without vortex dimensional crossover, but $Ca_{10}(Pt_3As_8)((Fe_{0.92}Pt_{0.08})_2As_2)_5$ shows the crossover from 3D vortex glass to 2D vortex liquid. This seems to be due to the temperature dependence of anisotropy γ, but in order to confirm this, a band calculation considering the many-body effect is required.

CRediT authorship contribution statement

W.J. Choi: Data curation, Formal analysis, Software, Investigation, Methodology, Writing - original draft. **Y.I. Seo:** Data curation, Visualization. **D. Ahmad:** Validation, Writing - original draft. **Y.S. Kwon:** Funding acquisition, Project administration, Supervision, Writing - review & editing.

Declaration of Competing Interest

The authors declare that they have no known competing financial interests or personal relationships that could have appeared to influence the work reported in this paper.

Acknowledgement

References

[1] Ni N, Allred JM, Chan BC, Cava RJ. High $T(c)$ electron doped $Ca_{10}(Pt_3As_8)(Fe_2As_2)_5$ and $Ca_{10}(Pt_4As_8)(Fe_2As_2)_5$ superconductors with skutterudite intermediary layers. PNAS 2011;108:E1019. https://doi.org/10.1073/pnas.1110563108.

[2] Seo YI, Choi WJ, Kimura SI, Bang Y, Kwon YS. Optical properties of optimally doped single-crystal $Ca_{8.5}La_{1.5}(Pt_3As_8)(Fe_2As_2)_5$. Phys Rev B 2017;95:094510. https://doi.org/10.1103/PhysRevB.95.094510.

[3] Cho K, Tanatar MA, Kim H, Straszheim WE, Ni N, Cava RJ, et al. Doping-dependent superconducting gap anisotropy in the two-dimensional pnictide $Ca_{10}(Pt_3As_8)$ $[(Fe_{1-x}Pt_x)_2As_2]_5$. Phys Rev B 2012;85:020504(R). https://doi.org/10.1103/PhysRevB.85.020504.

[4] Ni N, Straszheim WE, Williams DJ, Tanatar MA, Prozorov R, Bauer ED, et al. Transport and thermodynamic properties of $(Ca_{1-x}La_x)_{10}(Pt_3As_8)(Fe_2As_2)_5$ superconductors. Phys Rev B 2013;87:060507(R). https://doi.org/10.1103/PhysRevB.87.174507.

[5] Xiang ZJ, Luo XG, Ying JJ, Wang XF, Yan YJ, Wang AF, et al. Transport properties and electronic phase diagram of single-crystalline $Ca_{10}(Pt_3As_8)((Fe_{1-x}Pt_x)_2As_2)_5$. Phys Rev B 2012;85:224527. https://doi.org/10.1103/PhysRevB.85.224527.

[6] Ding QP, Tsuchiya Y, Sun Y, Taen T, Nakajima Y, Tamegai T. Anisotropies and homogeneities of superconducting properties in iron-platinum-arsenide $Ca_{10}(Pt_3As_8)(Fe_{1.79}Pt_{0.21}As_2)_5$. J Phys Soc Jpn 2012;81:114723. https://doi.org/10.1143/JPSJ.81.114723.

[7] Kim J, Ronning F, Haberkorn N, Civale L, Nazaretski E, Ni N, et al. Large magnetic penetration depth and thermal fluctuations in a superconducting $Ca_{10}(Pt_3As_8)$ $[(Fe_{1-x}Pt_x)_2As_2]_5$ (x=0.097) single crystal. Phys Rev B 2012;85:180504-R. https://doi.org/10.1103/PhysRevB.85.180504.

[8] Seo YI, Choi WJ, Ahmad D, Kimura SI, Kwon YS. Temperature dependence of the superconducting energy gaps in $Ca_{9.35}La_{0.65}(Pt_3As_8)(Fe_2As_2)_5$ single crystal. Sci Rep 2018;8:8648. https://doi.org/10.1038/s41598-018-24940-9.

[9] Damascelli A, Hussain Z, Shen ZX. Angle-resolved photoemission studies of the cuprate superconductors. Rev Mod Phys 2003;75:473. https://doi.org/10.1103/RevModPhys.75.473.

[10] Sterne PA, Wang CS. Higher T_c through metallic inter-layer coupling in $Bi_2Sr_2CaCu_2O_8$. J Phys C 1988;21:L949. https://doi.org/10.1088/0022-3719/21/26/005.

[11] Sheng ZZ, Hermann AM, El Ali A, Almasan C, Estrada J, Datta T, et al. Superconductivity at 90 K in the Tl-Ba-Cu-O system. Phys Rev Lett 1988;60:937. https://doi.org/10.1103/PhysRevLett.60.937.

[12] Parkin SSP, Lee VY, Engler EM, Nazzal AI, Huang TC, Gorman G, et al. Bulk superconductivity at 125 K in $Tl_2Ca_2Ba_2Cu_3O_x$. Phys Rev Lett 1988;60:2539. https://doi.org/10.1103/PhysRevLett.60.2539.

[13] Gao L, Huang ZJ, Meng RL, Lin JG, Chen F, Beauvais L, et al. Study of superconductivity in the Hg-Ba-Ca-Cu-O system. Physica C 1993;213:261. https://doi.org/10.1016/0921-4534(93)90440-2.

[14] Mikitik GP, Brandt EH. Peak effect, vortex-lattice melting line, and order-disorder transition in conventional and high-T_c superconductors. Phys Rev B 2001;64:184514. https://doi.org/10.1103/PhysRevB.64.184514.

[15] Pallecchi I, Fanciulli C, Tropeano M, Palenzona A, Ferretti M, Malagoli A, et al. Upper critical field and fluctuation conductivity in the critical regime of doped SmFeAsO. Phys Rev B 2009;79:104515. https://doi.org/10.1103/PhysRevB.79.104515.

[16] Lei H, Wang K, Hu R, Ryu H, Abeykoon M, Bozin ES, et al. Iron chalcogenide superconductors at high magnetic fields. Sci Technol Adv Mater 2012;13:054305. https://doi.org/10.1088/1468-6996/13/5/054305.

[17] Ge J, Gutierrez J, Li J, Yuan J, Wang HB, Yamaura K, et al. Dependence of the flux-creep activation energy on current density and magnetic field for a $Ca_{10}(Pt_3As_8)$ $[(Fe_{1-x}Pt_x)_2As_2]_5$ single crystal. Appl Phys Lett 2014;104:112603. https://doi.org/10.1063/1.4868871.

[18] Singh SJ, Bristow M, Meier WR, Taylor P, Blundell SJ, Canfield PC, et al. Ultrahigh critical current densities, the vortex phase diagram, and the effect of granularity of the stoichiometric high-T_c superconductor $CaKFe_4As_4$. Phys. Rev. Mater. 2018;2:074802. https://doi.org/10.1103/PhysRevMaterials.2.074802.

[19] Kumar A, Ghosh S, Tamegai T, Banerjee SS. Low-field vortex melting in a single crystal of $Ba_{0.6}K_{0.4}Fe_2As_2$. Phys Rev B 2020;101:014502. https://doi.org/10.1103/PhysRevB.101.014502.

[20] Surmach MA, Brückner F, Kamusella S, Sarkar R, Portnichenko PY, Park JT, et al. Superconducting properties and pseudogap from preformed Cooper pairs in the triclinic $(CaFe_{1-x}Pt_xAs)_{10}Pt_3As_8$. Phys Rev B 2015;91:104515. https://doi.org/10.1103/PhysRevB.91.104515.

[21] Bean CP. Magnetization of high-field superconductors. Rev Mod Phys 1964;36:31. https://doi.org/10.1103/RevModPhys.36.31.

[22] Yang H, Luo H, Wang Z, Wen HH. Fishtail effect and the vortex phase diagram of single crystal $Ba_{0.6}K_{0.4}Fe_2As_2$. Appl Phys Lett 2008;93:142506. https://doi.org/10.1063/1.2996576.

[23] Ding QP, Tsuchiya Y, Mohan S, Taen T, Nakajima Y, Tamegai T. Magnetic and transport properties of iron-platinum arsenide $Ca_{10}(Pt_{4-δ}As_8)(Fe_{2-x}Pt_xAs_2)_5$ single crystal. Phys Rev B 2012;85:104512. https://doi.org/10.1103/PhysRevB.85.104512.

[24] Zhang YZ, Wen HH, Wang Z. Thermally activated energies of $YBa_2Cu_3O_{7-δ}$ and $Y_{0.8}Ca_{0.2}Ba_2Cu_3O_{7-δ}$ thin films. Phys Rev B 2006;74:144521. https://doi.org/10.1103/PhysRevB.74.144521.

[25] Zhang YZ, Ren ZA, Zhao ZX. Thermally activated energy and critical magnetic fields of $SmFeAsO_{0.9}F_{0.1}$. Supercond Sci Technol 2009;22:065012. https://doi.org/10.1088/0953-2048/22/6/065012.

[26] Blatter G, Feigel'Man MV, Geshkenbein VB, Larkin AI, Vinokur VM. Vortices in high-temperature superconductors. Rev Mod Phys 1994;66:1125. doi:10.1103/RevModPhys.66.1125.

[27] López D, Krusin-Elbaum L, Safar H, Righi E, De la Cruz E, Grigera S, et al. Pinned vortex liquid above the critical point of the first-order melting transition: a consequence of pointlike disorder. Phys Rev Lett 1998;80:1070. https://doi.org/10.1103/PhysRevLett.80.1070.

[28] Song J, Kang B, Rhee JS, Kwon YS. Thermally activated flux flow and fluctuation conductivity in LiFeAs single crystal. EPL (Europhys Lett) 2012;97:47003. doi:10.1209/0295-5075/97/47003.

[29] Tinkham M. Resistive transition of high-temperature superconductors. Phys Rev Lett 1988;61:1658. https://doi.org/10.1103/PhysRevLett.61.1658.

[30] Wang ZH, Cao XW. The effective activation energy $U_e(T,H)$ in epitaxial $GdBa_2Cu_3O_{7-δ}$ thin films. Solid State Commun 1999;109:709. https://doi.org/10.1016/S0038-1098(98)00573-0.

[31] Kim DH, Gray KE, Kampwirth RT, McKay DM. Possible origins of resistive tails and critical currents in high-temperature superconductors in a magnetic field. Phys Rev B 1990;42:6249. https://doi.org/10.1103/PhysRevB.42.6249.

[32] Chong SV, Williams GVM, Sambale S, Kadowaki K. Doping dependence of the upper critical field, superconducting current density and thermally activated flux flow activation energy in polycrystalline $CeFeAsO_{1-x}F_x$ superconductors. Physica C 2014;507:35. https://doi.org/10.1016/j.physc.2014.09.015.

[33] Wang XL, Ghorbani SR, Lee SI, Dou SX, Lin CT, Johansen TH, et al. Very strong intrinsic flux pinning and vortex avalanches in $(Ba, K)Fe_2As_2$ superconducting single crystals. Phys Rev B 2010;82:024525. https://doi.org/10.1103/PhysRevB.82.024525.

[34] Xing XZ, Li ZF, Yi XL, Feng JJ, Xu CQ, Zhou N, et al. Thermally activated flux flow, vortex-glass phase transition and the mixed-state Hall effect in 112-type iron pnictide superconductors. Sci China-Phys Mech Astron 2018;61:127406. https://doi.org/10.1007/s11433-018-9280-6.

[35] Wu Z, Tao J, Xu X, Qiu L, Yang S, Wang Z. Anisotropic flux pinning energy in $FeSe_xTe_{1-x}$ single crystals. Physica C 2016;528:39. https://doi.org/10.1016/j.physc.2016.07.004.

[36] Lei H, Hu R, Choi ES, Petrovic C. Thermally activated energy and flux-flow Hall effect of $Fe_{1+y}(Te_{1+x}S_x)_z$. Phys Rev B 2010;82:134525. https://doi.org/10.1103/PhysRevB.82.134525.

[37] Choi WJ, Seo YI, Ahmad D, Kwon YS. Thermal activation energy of 3D vortex matter in $NaFe_{1-x}Co_xAs$ (x = 0.01, 0.03 and 0.07) single crystals. Sci Rep 2017;7:10900.

[38] Fisher MPA. Vortex-glass superconductivity: a possible new phase in bulk High-T_c oxides. Phys Rev Lett 1989;62:1415. https://doi.org/10.1103/PhysRevLett.62.1415.

[39] Liu SL, Wu GJ, Xu XB, Wu J, Shao HM. Scaling of the vortex-liquid resistivity in high temperature superconductors. Supercond Sci Technol 2005;18:1332. https://doi.org/10.1088/0953-2048/18/10/014.

[40] Hänisch J, Iida K, Ohmura T, Matsumoto T, Hatano T, Langer M, et al. Vortex glass-liquid transition and activated flux motion in an epitaxial, superconducting NdFeAs(O, F) thin film. MRS Commun 2018;8:1433. https://doi.org/10.1557/mrc.2018.207.

[41] Lee HS, Bartkowiak M, Kim JS, Lee HJ. Magnetic-field-induced crossover of vortex-line coupling in $SmFeAsO_{0.85}$ single crystal. Phys Rev B 2010;82:104523. https://doi.org/10.1103/PhysRevB.82.104523.

[42] Safar H, Gammel PL, Bishop DJ, Mitzi DB, Kapitulnik A. SQUID picovoltometry of single crystal $Bi_2Sr_2CaCu_2O_{8+\delta}$: observation of the crossover from high-temperature Arrhenius to low-temperature vortex-glass behavior. Phys Rev Lett 1992;68:2672. https://doi.org/10.1103/PhysRevLett.68.2672.

[43] Fischer KH. Vortices in high-T_c superconductors. Supercond Rev 1995;1:153.